Processing and Application of Ceramics 19 [1] (2025) 26–35
https://doi.org/10.2298/PAC2501026H

Exploring the correlation of structure and microwave dielectric performance in metal-doped $CaTiO_3$-$SmAlO_3$ ceramics

Yang Hu*

Lam Research Corporation, Fremont, CA 94538, USA

Received 28 October 2024; Received in revised form 26 December 2024; Accepted 31 January 2025

Abstract

$CaTiO_3$-$SmAlO_3$ ceramics, doped with metal ions (Cu, Zn or Ni), were prepared through a thermal decomposition method and sintering at 1370 °C. A comprehensive analysis of the microstructure and dielectric properties was conducted. Structural and morphological characteristics of the specimens were studied using X-ray diffraction (XRD) and scanning electron microscopy (SEM). The Rietveld refinement of XRD data indicated the presence of a single solid solution phase in all samples. SEM images revealed dense structure with well-identified grains of the $CaTiO_3$-$SmAl_{1-x}R_xO_3$ (R = Cu, Zn or Ni; x = 0.005, 0.010, 0.015) ceramics. Raman spectroscopy was employed to detect the degree of short-range ordering. Microwave dielectric characteristics and their structural origin, including dielectric constant (ε_r), quality factor ($Q\times f$), and temperature coefficient (τ_f), were thoroughly investigated. The study evaluated porosity, polarizability, bond valency, grain size, short-range ordering and tolerance factor, discussing their relationships with microwave dielectric properties. The investigation established the correlation between microstructure and dielectric characteristics, highlighting the primary factors influencing the quality factor and temperature coefficient. Notably, the $CaTiO_3$-$SmAl_{0.99}Zn_{0.01}O_3$ sample, doped with 1.0 at.% Zn, exhibited a high quality factor ($Q\times f$) of 44700 GHz and a dielectric constant (ε_r) of 39.6.

Keywords: *microwave dielectric ceramics, $CaTiO_3$-$SmAlO_3$, microstructure, dielectric properties*

I. Introduction

The rapid advancements in the wireless communications industry, satellite broadcasting, intelligent transport systems (ITS) and energy storage applications have driven the increasing demand for compact dielectric resonators with enhanced frequency selectivity and temperature stability. Early dielectric resonators, however, were characterized by large volumes, making them unsuitable for microwave integrated circuits. The surge in the wireless communications sector has heightened the need for smaller dielectric resonators with high quality factors and reliable temperature performance. In recent years, dielectric ceramics have garnered substantial interest due to their outstanding performance, including high dielectric constants (ε_r), high quality factors ($Q\times f$) and low temperature coefficients (τ_f). Achieving optimal dielectric ceramic material that simultaneously satisfies these three properties is a challenging task [1,2].

Among these ceramics, the $CaTiO_3$ system has gained significant attention due to its versatility in a wide range of applications. $CaTiO_3$ exhibits a distorted orthorhombic structure, a high dielectric constant (ε_r > 170), a moderate quality factor ($Q\times f \sim 7000$ GHz) and a high positive temperature coefficient (τ_f > 800 ppm/°C) [3]. However, a pure $CaTiO_3$ ceramics' low quality factor and high temperature coefficient pose challenges in meeting practical production requirements.

Numerous solid solutions based on $CaTiO_3$ have been proposed to suppress the large positive temperature coefficient of resonance frequency (τ_f). For instance, Zhou *et al.* [4] reported that CeO_2-added $CaTiO_3$-$SmAlO_3$ ceramics, prepared by the reaction sintering method, demonstrated excellent microwave dielectric characteristics: $\varepsilon_r \sim 43.9$, $Q\times f \sim 48779$ GHz and $\tau_f \sim -0.24$ ppm/°C. Mohapatra *et al.* [5] systematically studied (1-x)$MgTiO_3$-$xCaTiO_3$ ceramics for dielectric resonator applications and achieved dielectric properties of $\varepsilon_r \sim 13.03$, $Q\times f \sim 29458$ GHz and

*Corresponding authors: tel: +1 510 731 8199,
e-mail: *yang.hu@lamresearch.com*, *hu_yang1990@hotmail.com*

tuneable $\tau_f \sim -0.18$ ppm/°C. Hu *et al.* [6] examined rare earth ion-doped $CaTiO_3$-$SmAlO_3$ ceramics and found that the $CaTiO_3$-$Sm_{0.85}Nd_{0.15}AlO_3$ sample, doped with 1.5 at.% Ce, exhibited a relative dielectric constant of $\varepsilon_r \sim 39.3$, the highest quality factor of $Q\times f$ = 49430 GHz and a small temperature coefficient of $\tau_f \sim -9.4$ ppm/K. Wang *et al.* [7] studied cold-sintered $CaTiO_3$-K_2MoO_4 microwave dielectric ceramics and achieved a near-zero τ_f for $CaTiO_3$-$0.92K_2MoO_4$ composites with $\varepsilon_r \sim 8.5$ and $Q\times f \sim 11000$ GHz. Hu *et al.* [8] explored Mg_2TiO_4-$MgTiO_3$-$CaTiO_3$ ceramics over a wide temperature range and discovered that the $0.32Mg_2TiO_4$-$0.611MgTiO_3$-$0.069CaTiO_3$ ceramics exhibited better dielectric temperature stability, with properties of ε_r = 19.7, $Q\times f$ = 55400 GHz (at 8.43 GHz), τ_f = 4.5 ppm/°C (in temperature range from −40 to 25 °C) and τ_f = −5.1 ppm/°C (in temperature range from 25 to 90 °C) [8]. Du *et al.* [9] fabricated wideband low-profile dielectric patch antennas from temperature-stable $0.65CaTiO_3$-$0.35LaAlO_3$ ceramics, achieving dielectric properties of $\varepsilon_r \sim 44.8$, $Q\times f \sim 43950$ GHz at 3.67 GHz and $\tau_f \sim 0$ ppm/°C. Uddin *et al.* [10] investigated a new lead-free composition of $Ca(Ti_{1-x}Zr_x)O_3$ ceramics and found that $CaZrO_3$ ceramics achieved a quality factor (Q) value of 3267 GHz, while the maximum quality factor (~8400 GHz) was obtained for x = 0.5. Zhou *et al.* [11] studied $CaTiO_3$-$LnAlO_3$ (Ln = La, Nd) ceramics and achieved excellent performance with ε_r = 39.1, $Q\times f$ = 45635 GHz and τ_f = −1.48 ppm/°C as well as ε_r = 44.03, $Q\times f$ = 46269 GHz and τ_f = 2.63 ppm/°C. Song *et al.* [11] examined $CaTiO_3$-$La(Mg_{2/3}Nb_{1/3})O_3$ ceramics, achieving $\varepsilon_r = 23.65 \pm 0.2$, $Q\times f = 33517 \pm 2000$ GHz at 7.8 GHz and $\tau_f = -79.7 \pm 2.0$ ppm/°C. Masin *et al.* [12] studied $0.95(Mg_{0.95}Zn_{0.05})TiO_3$-$0.05CaTiO_3$ ceramics and obtained $\varepsilon_r \sim 19.8$, $\tau_f < -6$ ppm/°C and $Q\times f$ = 69600 GHz. Zaman *et al.* [13] investigated $Ca(Hf_xTi_{1-x})O_3$ ceramics and found that substituting Hf^{4+} ions for Ti^{4+} resulted in a decrease in the microwave dielectric constant (ε_r) from 145 to 52, while the quality factor ($Q\times f$) increased from 8105 to 24305 GHz and the temperature coefficient of resonant frequency tuned towards zero ($\tau_f \sim 4.5$ ppm/°C). Pei *et al.* [14] investigated the fabrication and microwave dielectric performance of $Li_4Mg_2SbO_6F$ ceramics through a solid-state sintering process, resulting in optimal performance at 750 °C with ε_r = 12.6, $Q\times f$ = 59000 GHz (at 11.3 GHz), τ_f = −37.0 ppm/K and successful application in a dielectric resonator antenna [14]. Zhang *et al.* [15] explored the synthesis and dielectric properties of CaB_2O_4 ceramics, demonstrating that varying Ca/B ratios and the addition of boron and TiO_2 improve densification and dielectric performance, with optimal properties of ε_r = 6.03, $Q\times f$ = 37962 GHz and τ_f = −24.7 ppm/°C achieved at 950 °C for both pure and composite ceramics. Ma *et al.* [16] showed $Mg_3Ga_2TiO_8$ ceramics prepared by a solid-phase method, highlighting their exceptional microwave dielectric properties: ε_r = 12.07, $Q\times f$ = 89270 GHz and τ_f = −40.7 ppm/°C. Lin *et al.* [17] studied TiO_2-doped $CaNb_2O_6$ ceramics prepared by solid-state reaction, highlighting the impact of Ti^{4+} on lattice site substitution, oxygen vacancies and dielectric properties, achieving optimal microwave performance with ε_r = 15.76, $Q\times f$ = 30397 GHz, τ_f = −22 ppm/°C at 1425 °C for x = 0.02. Yuan *et al.* [18] investigated enhancing the mechanical properties and dielectric performance of high-entropy $R(Nb_{1-x}Ta_x)_2O_6$ ceramics, prepared by solid-phase reaction, emphasizing the impact of Ta^{5+} content on grain size, dielectric properties and mechanical robustness. Xiang *et al.* [19] studied high-entropy $[(Mg_{1/2}Zn_{1/2})_{0.4+x}(Ni_{1/3}Co_{1/3}Mn_{1/3})_{0.6-x}]_2TiO_4$ ceramics, highlighting their phase compositions, microstructures and optimal microwave dielectric properties achieved with varying x values, emphasizing the influence of ion polarization, packing fraction and A-site bond strength. Jiang *et al.* [20] studied microwave dielectric $Zn_{1.8}SiO_{3.8}$ ceramics doped with rare earth elements (La, Pr, Nd, Sm) and observed improved dielectric properties and densification at lower temperatures in Nd-doped sample, exhibiting the best performance with ε_r = 7.02, $Q\times f$ = 127711 GHz and τ_f = −33.52 ppm/ °C.

In this study, $CaTiO_3$-$SmAlO_3$ ceramics doped with metal ions (Cu, Zn, Ni) were prepared using the thermal decomposition method and sintering at 1370 °C. Detailed analysis of the ceramics' microstructure and dielectric properties were conducted. The study thoroughly investigated the microwave dielectric characteristics, including dielectric constant (ε_r), quality factor ($Q\times f$) and temperature coefficient (τ_f). This investigation highlighted the correlation between microstructure and dielectric characteristics, identifying the key factors in improving the quality factor. Specifically, the $CaTiO_3$-$SmAl_{0.99}Zn_{0.01}O_3$ sample, doped with 1.0 at.% Zn, demonstrated a high $Q\times f$ of 44700 GHz, a dielectric constant of 39.6 and a temperature coefficient of −7.9 ppm/°C.

II. Experimental

This work investigates $CaTiO_3$-$SmAl_{1-x}R_xO_3$ systems, where R is Cu, Zn or Ni, and x signifies the doping concentration (refer to Table 1). The samples were synthesized using the precursor thermal decomposition method. In the beginning, $CaCO_3$ and TiO_2, with a purity of over 99% (Wuxi Xishenghuilong Company), were mechanically milled with ZrO_2 balls in deionized water for 6 h. In a separate batch, Sm_2O_3, Al_2O_3 and metal oxides (CuO, ZnO and NiO), also with a purity of over 99% (Wuxi Xishenghuilong Company), underwent mechanical milling with ZrO_2 balls in deionized water for 6 h.

After the drying process, two powders were combined and calcined at 950 °C for 3 h. The calcined pow-

Table 1. $CaTiO_3$-$SmAl_{1-x}R_xO_3$ (R = Cu, Zn, Ni) sample name and molecular formula

Sample name	Composition
SA-0	$CaTiO_3$-$SmAlO_3$
SA-Cu-5	$CaTiO_3$-$SmAl_{0.995}Cu_{0.005}O_3$
SA-Cu-10	$CaTiO_3$-$SmAl_{0.99}Cu_{0.01}O_3$
SA-Cu-15	$CaTiO_3$-$SmAl_{0.985}Cu_{0.015}O_3$
SA-Zn-5	$CaTiO_3$-$SmAl_{0.995}Zn_{0.005}O_3$
SA-Zn-10	$CaTiO_3$-$SmAl_{0.99}Zn_{0.01}O_3$
SA-Zn-15	$CaTiO_3$-$SmAl_{0.985}Zn_{0.015}O_3$
SA-Ni-5	$CaTiO_3$-$SmAl_{0.995}Ni_{0.005}O_3$
SA-Ni-10	$CaTiO_3$-$SmAl_{0.99}Ni_{0.01}O_3$
SA-Ni-15	$CaTiO_3$-$SmAl_{0.985}Ni_{0.015}O_3$

ders were then blended with a 5 wt.% PVA (polyvinyl alcohol) binder and uniaxially pressed into disks with a diameter of 10 mm and a thickness of 6 mm, applying a pressure of 200 MPa. Subsequently, the ceramic disks underwent initial heat treatment, gradually raising the temperature at a rate of 5 °C/min to 600 °C, holding for 60 min, and then sintering at 1370 °C for 3 h. For each composition, three samples were fabricated to ensure repeatability and to obtain standard deviation estimates for the dielectric constant and quality factor.

The density of sintered samples was determined using the Archimedes method. X-ray diffraction (D/Max-2500, Rigakku, Tokyo, Japan) was employed to characterize the crystal structures. XRD measurements were taken across a broad range of Bragg's angle 2θ ($20° \leq 2\theta \leq 80°$) with a step size of 0.02°, using Cu-Kα radiation (λ = 1.5405 Å). The Rietveld refinement technique, utilizing the GSAS application, was used to determine the lattice parameters and profile fitting [21,22]. The relative density (ρ_{rel}) was calculated using the measured density (ρ_{mea}), determined by the Archimedes method, and the theoretical density (ρ_{the}), obtained from XRD refinement:

$$\rho_{rel} = \frac{\rho_{mea}}{\rho_{the}} \times 100 \quad (1)$$

Microstructure analysis was performed using scanning electron microscopy (SEM, JSM-6301F, JEOL, Tokyo, Japan) and Raman spectroscopy (HR800, Horiba Jobin Yxon, Villenece D'ascq, France). Dielectric properties were assessed using a precision impedance analyser (HP8720ES, Hewlett-Packard, Santa Rosa, CA). The dielectric constant was determined using the Hakki-Coleman method and the temperature coefficient (in ppm/ °C) was calculated by capturing resonance frequencies at various temperatures, using the following formula:

$$\tau_f = \frac{f_1 - f_2}{f_1(T_2 - T_1)} \times 10^6 \quad (2)$$

where f_1 and f_2 represent the resonant frequency at T_1 (25 °C) and T_2 (80 °C), respectively.

III. Results and discussion

Figure 1 presents the XRD spectra of $CaTiO_3$-$SmAl_{1-x}R_xO_3$ (R = Cu, Zn, Ni; x = 0.05, 0.010 and 0.015) collected at room temperature using Cu-Kα radiation (λ = 1.5405 Å). Previous studies [23,24] have shown that both $CaTiO_3$ and $SmAlO_3$ possess an orthorhombic structure with the *Pbnm* space group at room temperature. For phase identification, all XRD diffraction peaks for $CaTiO_3$ (PDF #42-0423) are included to confirm the phase composition. The results revealed that all specimens displayed a pure orthorhombic structure with the *Pbnm* space group. Prominent peaks corresponding to the perovskite phase, such as 121, 202, 040 and 004, were observed in all spectra. No secondary phases were detected within the observation range, confirming the formation of solid solutions. The Rietveld refinement method, using the GSAS application, was utilized to analyse the measurements as shown in Fig. 2. The Rietveld method employs the least squares approach to fit the calculated profile with the experimental XRD data points. During the refinement process, parameters such as the scale factor, unit cell parameters, thermal parameters, atomic positions and peak shape parameters were adjusted. The XRD data background was modelled using a polynomial function. The fitted curves closely matched the measured data points, indicating a high degree of accuracy. The refined lattice parameters and goodness of fit parameters are summarized in Table 2. Due to the low concentration of dopants, the lattice constant and cell volume remained largely unaffected by the doping levels in all samples.

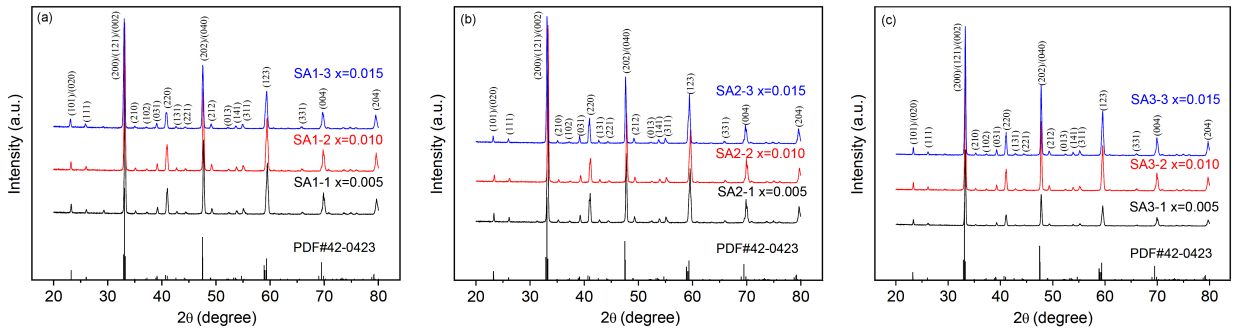

Figure 1. XRD patterns of: a) $CaTiO_3$-$SmAl_{1-x}Cu_xO_3$, b) $CaTiO_3$-$SmAl_{1-x}Zn_xO_3$ and c) $CaTiO_3$-$SmAl_{1-x}Ni_xO_3$ (where x = 0.005, 0.010, 0.015)

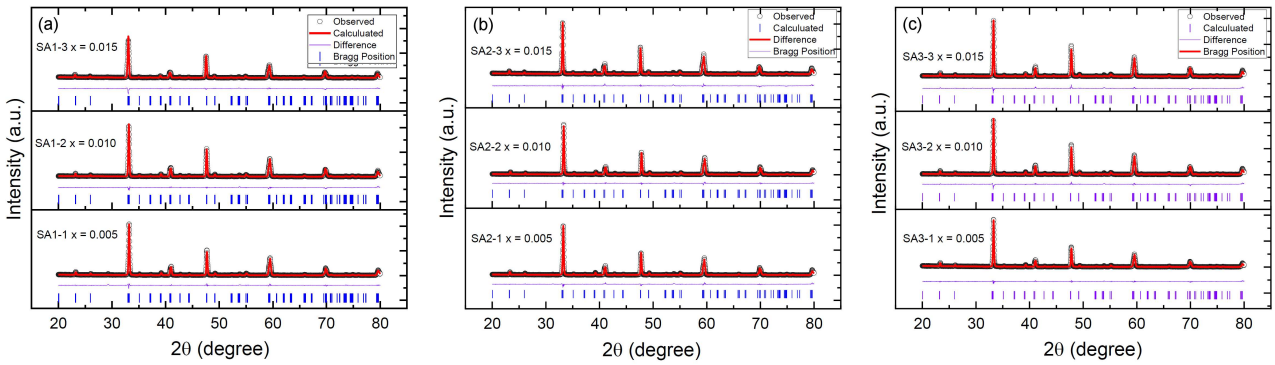

Figure 2. The Rietveld refinement plots of: a) $CaTiO_3$-$SmAl_{1-x}Cu_xO_3$, b) $CaTiO_3$-$SmAl_{1-x}Zn_xO_3$ and c) $CaTiO_3$-$SmAl_{1-x}Ni_xO_3$ (where x = 0.005, 0.010, 0.015)

Table 2. Crystal symmetry, lattice constant, cell volume and goodness of fit of Rietveld refinements of sintered $CaTiO_3$-$SmAl_{1-x}R_xO_3$ (R = Cu, Zn, Ni) samples

Sample	Symmetry	a [Å]	b [Å]	c [Å]	Cell volume [Å^3]	χ^2
SA-0	*Pbnm*	5.393	7.593	5.361	219.54	2.30
SA-Cu-5		5.399	7.595	5.364	219.99	2.32
SA-Cu-10	*Pbnm*	5.412	7.619	5.370	221.45	2.38
SA-Cu-15		5.403	7.598	5.363	220.20	2.33
SA-Zn-5		5.395	7.594	5.359	219.52	2.64
SA-Zn-10	*Pbnm*	5.398	7.598	5.362	219.94	2.15
SA-Zn-15		5.396	7.596	5.360	219.70	2.46
SA-Ni-5		5.394	7.596	5.364	219.81	2.10
SA-Ni-10	*Pbnm*	5.397	7.598	5.366	220.03	2.44
SA-Ni-15		5.396	7.598	5.367	220.02	2.45

The Goldschmidt's rule states that ions of one element can replace those of another in ionic crystals if their radii differ by less than approximately 15%. The ionic radius difference (ΔR) can be calculated using the equation:

$$\Delta R = \frac{|R_A - R_B|}{R_B} \times 100 \qquad (3)$$

where R_A and R_B denote the radii of the ions. The ΔR between Ca^{2+} (1.00 Å) and Sm^{3+} (1.079 Å) is 7.9%, and the ΔR between Ti^{4+} (0.605 Å) and Al^{3+} (0.535 Å) is 11.5%. The ΔR between Cu^{2+} (0.57 Å) and Al^{3+} (0.535 Å) is 6.5%, the ΔR between Zn^{2+} (0.6 Å) and Al^{3+} (0.535 Å) is 12.1%, and the ΔR between Ni^{2+} (0.55 Å) and Al^{3+} (0.535 Å) is 2.8%. Since the ionic radius differences are less than 15%, it suggests that a single perovskite phase can form, which has been confirmed by the XRD results.

The measured sample density and relative density of the $CaTiO_3$-$SmAl_{1-x}R_xO_3$ (R = Cu, Zn or Ni) ceramics are illustrated in Fig. 3. All samples exhibited a relative density exceeding 95% of the theoretical density, indicating high density after sintering. However, the Ni-doped samples displayed slightly lower relative density, as shown in Fig. 3c, with corresponding SEM images confirming the presence of small pores (see Figs. 4g-i). In contrast, Cu doping and Zn doping resulted in improved densification. The addition of CuO enhances densification due to the liquid phase sintering and increased grain boundary diffusivity [25]. Huang *et al.*

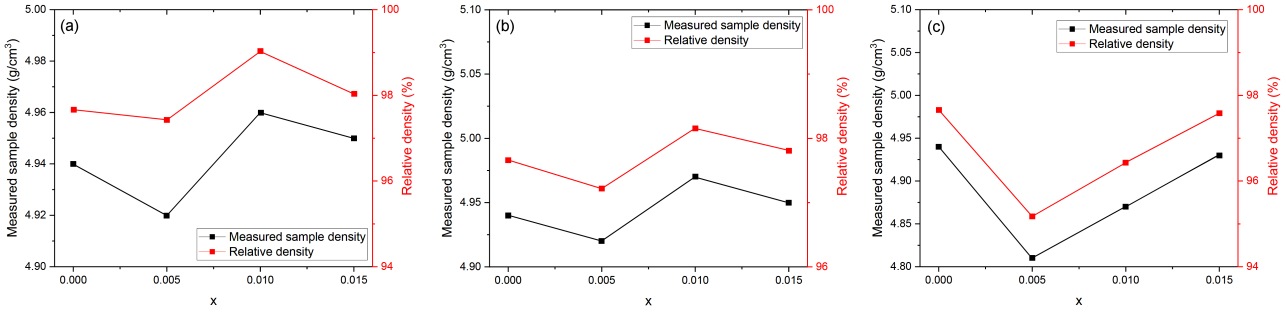

Figure 3. Measured sample density and relative density of: a) $CaTiO_3$-$SmAl_{1-x}Cu_xO_3$, b) $CaTiO_3$-$SmAl_{1-x}Zn_xO_3$ and c) $CaTiO_3$-$SmAl_{1-x}Ni_xO_3$ (where x = 0.005, 0.010, 0.015)

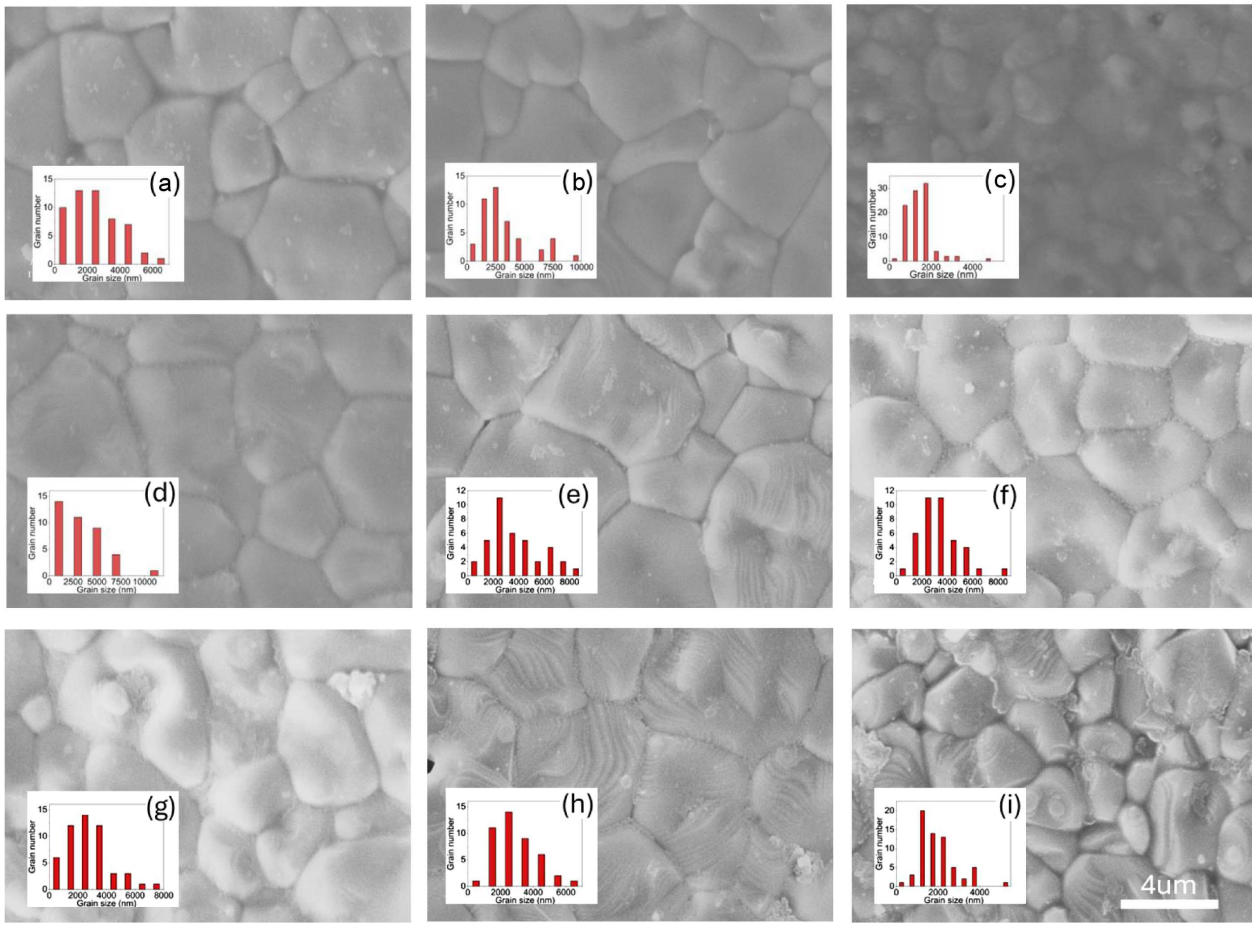

Figure 4. SEM images of: a-c) $CaTiO_3$-$SmAl_{1-x}Cu_xO_3$, d-f) $CaTiO_3$-$SmAl_{1-x}Zn_xO_3$, g-i) $CaTiO_3$-$SmAl_{1-x}Ni_xO_3$, where x = 0.005, 0.010, 0.015 (inset figure is the grain size distribution for each sample)

[26] also reported that ZnO addition effectively lowers the sintering temperature, promotes $Q \times f$ values, and inhibits the formation of secondary phases.

Figures 4a-c show the SEM micrographs and grain size distributions of the $CaTiO_3$-$SmAl_{1-x}Cu_xO_3$ (x = 0.005, 0.010, 0.015) specimens. Table 3 presents the average grain size of each sample. All samples are compact and well-densified, with the average grain size reducing from 3 μm to approximately 1.4 μm as the Cu doping amount increases. Figures 4d-f display the SEM micrographs and grain size distributions of the $CaTiO_3$-$SmAl_{1-x}Zn_xO_3$ (x = 0.005, 0.010, 0.015) specimens.

Table 3. $CaTiO_3$-$SmAl_{1-x}R_xO_3$ (R = Cu, Zn, Ni) and un-doped $CaTiO_3$-$SmAlO_3$ average grain size

Sample name	Average grain size [μm]
SA-0	2.14
SA-Cu-5	2.47
SA-Cu-10	3.09
SA-Cu-15	1.46
SA-Zn-5	3.49
SA-Zn-10	3.73
SA-Zn-15	3.47
SA-Ni-5	2.74
SA-Ni-10	2.94
SA-Ni-15	1.96

These samples exhibit equiaxed grains, with average grain sizes ranging from approximately 3.4 to 3.7 μm. The dense and uniform surface morphology aligns with the high relative density values shown in Table 4. Figures 4g-i illustrate the SEM micrographs and grain size distributions of the $CaTiO_3$-$SmAl_{1-x}Ni_xO_3$ (x = 0.005, 0.010, 0.015) specimens. In this case, the average grain size decreases from 2.7 to 1.9 μm with increased Ni doping, suggesting that Ni addition may adversely affect sinterability.

Raman spectroscopy is an effective tool for analysing the phase composition, chemical bond vibrations and cation distribution of dielectric materials. Figure 5 presents the Raman spectra of the $CaTiO_3$-$SmAl_{1-x}R_xO_3$ (R = Cu, Zn, Ni) ceramics with varying amounts of dopants. The low-frequency bands correspond to A–O movements [27,28], where the $CaTiO_3$ lattice mode should generate a band at 154 cm^{-1} [28]. However, due to the A-site substitution by heavy ion Sm^{3+}, the band shifts to lower frequency and cannot be detected [28]. The nearby band at 156 cm^{-1} (labelled T) reflects the translational vibration of A-site ions. The bands at 343 and 485 cm^{-1} (marked V1 and V2) are associated with the bending and internal vibration of the oxygen octahedra. The band around 785 cm^{-1}, characteristic of short-range ordering at B-site ions and recognized as the A_{1g}

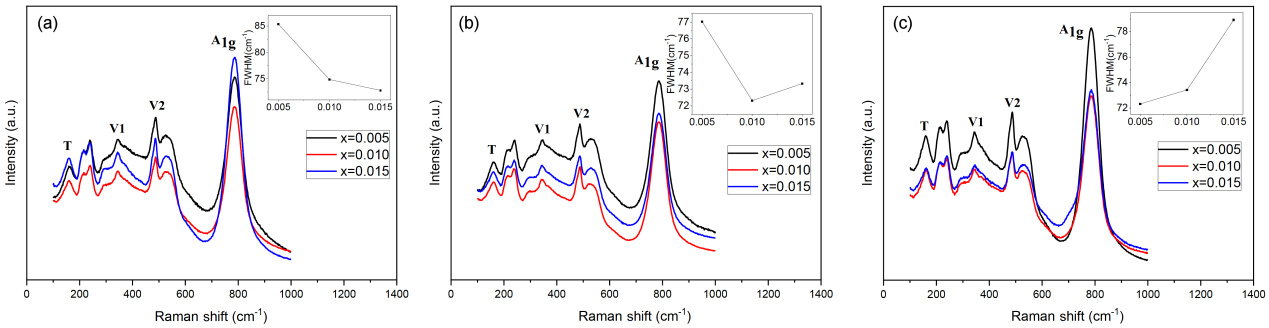

Figure 5. Raman spectra of: a) $CaTiO_3$-$SmAl_{1-x}Cu_xO_3$, b) $CaTiO_3$-$SmAl_{1-x}Zn_xO_3$, c) $CaTiO_3$-$SmAl_{1-x}Ni_xO_3$, where x = 0.005, 0.010, 0.015 (inset figure is the FWHM of A_{1g} peak for each sample)

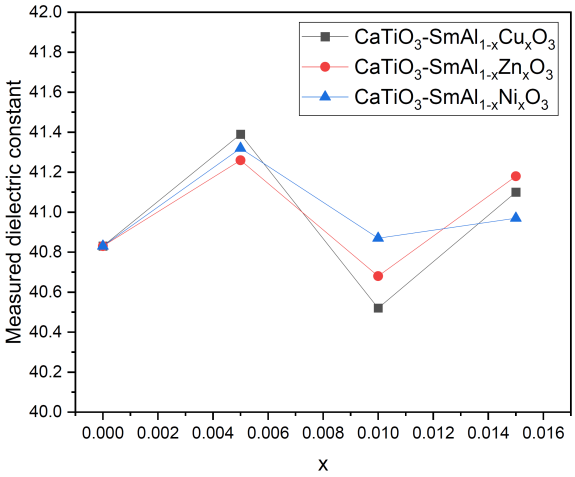

Figure 6. Measured dielectric constant ε_r after porosity correction for: a) $CaTiO_3$-$SmAl_{1-x}Cu_xO_3$, b) $CaTiO_3$-$SmAl_{1-x}Zn_xO_3$, c) $CaTiO_3$-$SmAl_{1-x}Ni_xO_3$ samples

mode, indicates the extent of short-range ordering in octahedral tilting [29,30]. The addition of Cu, Zn and Ni did not alter the positions of the Raman shifts but affected the sharpness and intensity of the A_{1g} mode. The Lorentz function fitting was utilized to calculate the full width at half-maximum (FWHM) of the 785 cm^{-1} band. The results (insets of Fig. 5) indicate that the FWHM narrows with increasing Cu content, reaches a minimum with 0.01 at.% Zn addition and widens with further Ni addition. This suggests that Cu addition enhances B-site ordering, while an optimal amount of Zn is necessary for achieving B-site ordering between Ti-Al-Zn. Increased Ni addition, however, distorts the Ti-Al-Ni short-range order.

Figure 6 and Table 4 present the measured dielectric constant of the specimens. The dielectric constant is influenced by several factors, including porosity, ion polarizability and impurity phases. Porosity in the sintered ceramic sample significantly impacts the dielectric constant (ε_r). Therefore, to determine the material's actual dielectric constant, the measured ε_r must be corrected for porosity. This correction can be made using the equation derived by Penn *et al.* [31]:

$$\varepsilon_r = \varepsilon_m \left(1 - \frac{3P(\varepsilon_m - 1)}{2\varepsilon_m + 1}\right) \tag{4}$$

The dielectric constant of the material adjusted for porosity, ε_r, is calculated using the experimental obtained dielectric constant, ε_m, and P is the fractional porosity derived from relative density. Table 4 and Fig. 6 display the porosity-corrected dielectric constant. With an increasing amount of Cu ion doping, the dielectric constant initially decreases from 41.39 to 40.52, then increases to 41.10. For Zn ion doping, the dielectric constant first decreases from 41.26 to 40.68, then rises to 41.18. Similarly, with Ni ion doping, the dielectric constant initially decreases from 41.32 to 40.87, then slightly increases to 40.97. The dielectric constant is

Table 4. Measured and corrected dielectric constant, quality factor, temperature coefficient and calculated dielectric constant of $CaTiO_3$-$SmAl_{1-x}R_xO_3$ (R = Cu, Zn, Ni)

Sample name	Measured ε_m	Corrected ε_r	Quality factor, $Q \times f$	Temperature coefficient, τ_f [ppm/°C]	Calculated ε_{thr}
SA-0	39.45	40.83	41324	−7.5	31.34
SA-Cu-5	39.85	41.39	41808.0	−7.0	30.73
SA-Cu-10	39.96	40.52	19934.5	−7.2	28.78
SA-Cu-15	39.93	41.10	9330.0	−8.0	30.55
SA-Zn-5	39.60	41.26	44089.5	−6.2	31.44
SA-Zn-10	39.60	40.68	44699.5	−7.9	30.86
SA-Zn-15	39.88	41.18	43940.5	−7.8	31.29
SA-Ni-5	38.44	41.32	37030.3	−4.5	30.96
SA-Ni-10	38.76	40.87	30315.3	−5.1	30.65
SA-Ni-15	39.54	40.97	26885.0	−5.2	30.69

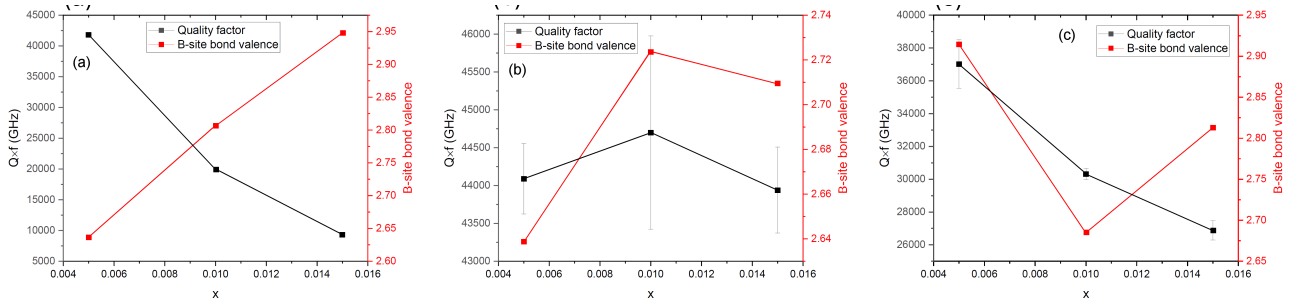

Figure 7. Quality factor and B-site bond valence of: a) $CaTiO_3$-$SmAl_{1-x}Cu_xO_3$, b) $CaTiO_3$-$SmAl_{1-x}Zn_xO_3$, c) $CaTiO_3$-$SmAl_{1-x}Ni_xO_3$ (where x = 0.005, 0.010, 0.015)

directly related to the polarizability per unit volume (α_m/V_m), as described by the Clausius-Mossotti formula:

$$\frac{\alpha_m}{V_m} = \frac{3(\varepsilon_{thr} - 1)}{4\pi(\varepsilon_{thr} + 2)} \tag{5}$$

where α_m represents the ionic polarizability, V_m is the refined cell volume, ε_{thr} is the dielectric constant. The polarizability α_m can be evaluated using the following formula:

$$\alpha_m = 0.65 \cdot [4\alpha(Ca^{2+}) + 4\alpha(Ti^{4+}) + 12\alpha(O^{2-})] + \\ + 0.35 \cdot [4\alpha(Sm^{3+}) + 4(1-x)\alpha(Al^{3+}) + 4x\alpha(R^{2+}) + \\ + 12\alpha(O^{2-})] \tag{6}$$

where R is Cu, Zn or Ni. According to Shanon *et al.* [32]: $\alpha(Ca^{2+})$ = 3.16 Å^3, $\alpha(Ti^{4+})$ = 2.93 Å^3, $\alpha(Sm^{3+})$ = 4.76 Å^3, $\alpha(Al^{3+})$ = 0.79 Å^3, $\alpha(O^{2-})$ = 2.01 Å^3, $\alpha(Cu^{2+})$ = 2.11 Å^3, $\alpha(Zn^{2+})$ = 2.04 Å^3 and $\alpha(Ni^{2+})$ = 1.23 Å^3.

Figure 6 and Table 4 show the theoretical dielectric constant, which has a strong correlation with the measured dielectric constant. The difference between theoretical and measured dielectric constants may be attributed to defects, such as grain boundaries and vacancies, in the specimens. These findings indicate that densification and polarizability per unit volume significantly influence the dielectric constant of the $CaTiO_3$-$SmAl_{1-x}R_xO_3$ (R = Cu, Zn, Ni) samples.

Figure 7 illustrates the variation in the quality factor ($Q\times f$) values of the $CaTiO_3$-$SmAl_{1-x}R_xO_3$ (R = Cu, Zn, Ni) with different doping levels. The $Q\times f$ values of the $CaTiO_3$-$SmAl_{1-x}Cu_xO_3$ ceramics (x = 0.005, 0.010, 0.015) range from 41808 to 9330 GHz, with the highest $Q\times f$ value of 41808 GHz achieved at a Cu ion addition of 0.5%. It is evident that $Q\times f$ values decrease as the Cu doping amount increases. For the $CaTiO_3$-$SmAl_{1-x}Zn_xO_3$ ceramics (x = 0.005, 0.010, 0.015), the $Q\times f$ values range from 43940 to 44699 GHz. The maximum $Q\times f$ value of 44699 GHz is obtained with a 1.0 at.% Zn ion addition. This trend shows an initial increase followed by a decrease with increasing Zn ion content. Similarly, for the $CaTiO_3$-$SmAl_{1-x}Ni_xO_3$ ceramics (x = 0.005, 0.010, 0.015), the $Q\times f$ values range from 26885 to 37030 GHz. The highest $Q\times f$ value of 37030 GHz is observed with a 0.5 at.% Ni ion addition. The $Q\times f$ values decrease with increasing Ni doping levels.

Figure 8 depicts the temperature coefficients of the resonant frequency (τ_f) for the $CaTiO_3$-$SmAl_{1-x}R_xO_3$ (R = Cu, Zn, Ni) ceramics with various doping levels (x = 0.005, 0.010, 0.015). All samples exhibit good thermal stability and low τ_f values. For the $CaTiO_3$-$SmAl_{1-x}Cu_xO_3$ ceramics, τ_f values range from −7.0 to −8.0 ppm/°C, decreasing with higher Cu doping levels. The $CaTiO_3$-$SmAl_{1-x}Zn_xO_3$ ceramics show τ_f values between −6.2 and −7.8 ppm/°C, also decreasing with increased Zn content. Similarly, the $CaTiO_3$-$SmAl_{1-x}Ni_xO_3$ ceramics have τ_f values ranging from −4.5 to −5.2 ppm/°C, with τ_f decreasing as Ni doping increases.

The quality factor ($Q\times f$) of microwave dielectric ceramics is influenced by both intrinsic and extrinsic losses. Extrinsic losses are caused by defects, porosities and secondary phases, while intrinsic losses arise from ionic vibrational modes related to the crystal structure's symmetry. To understand the extrinsic loss mechanism, X-ray diffraction combined with the Rietveld refinement is utilized to identify phase structure, cell

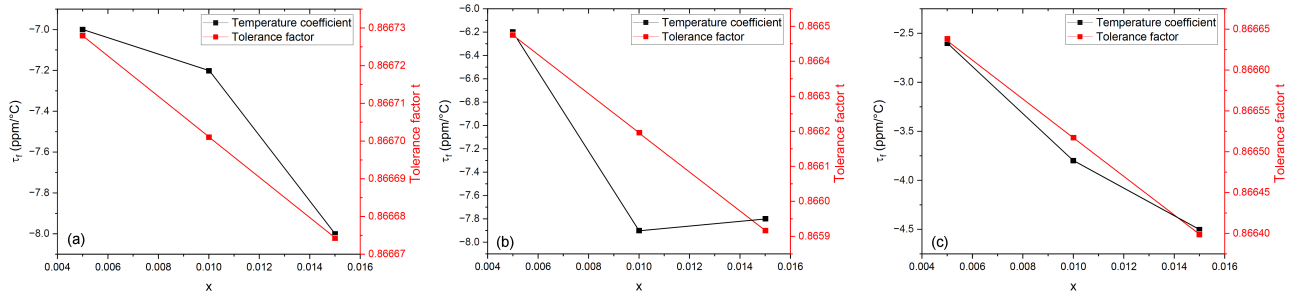

Figure 8. The temperature coefficient of resonant frequency of: a) $CaTiO_3$-$SmAl_{1-x}Cu_xO_3$, b) $CaTiO_3$-$SmAl_{1-x}Zn_xO_3$, c) $CaTiO_3$-$SmAl_{1-x}Ni_xO_3$ (where x = 0.005, 0.010, 0.015)

parameters, cell volume, and atomic positions. The XRD results and Rietveld refinement showed a single solid solution phase with an orthorhombic perovskite structure in all samples. Porosity was evaluated by the relative density, calculated from the measured sample density and cell volume obtained from XRD refinement. SEM imaging was employed to analyse grain morphology and size distribution. Grain boundaries, acting as 2D defects, were found to deteriorate the quality factor, correlating with grain size distribution [31,33]. For intrinsic loss mechanisms, Raman spectroscopy is employed to examine the degree of short-range ordering at the B-site, which correlates with the quality factor. Additionally, the quality factor is influenced by B-site bond valence, as reported by Kim *et al.* and Brown *et al.* [34,35]. The B-site bond valence can be calculated using the following equations:

$$S_{ij} = \exp\left(\frac{r_0 - r}{B}\right) \tag{7}$$

$$V_i = \sum_j S_{ij} \tag{8}$$

where S_{is} the bond valence between ions i and j, r_0 and B are empirically determined parameters based on ion species of i and j, r is the bond length between ions i and j. The V_i is the total bond valence which sums all B–O bonds. The bond length r can be obtained from XRD Rietveld refinement results. According to the literature data [35,36], empirical parameter have the following values: r_0(Ca–O) = 1.967 Å, r_0(Sm–O) = 2.055 Å, r_0(Ti–O) = 1.815 Å, r_0(Al–O) = 1.651 Å, r_0(Cu–O) = 1.679 Å, r_0(Zn–O) = 1.704 Å and r_0(Ni–O) = 1.654 Å. B is a constant number of 0.37. The calculated B-site bond valence for the $CaTiO_3$-$SmAl_{1-x}R_xO_3$ (R = Cu, Zn, Ni) ceramics with various doping levels (x = 0.005, 0.010, 0.015) is plotted in Fig. 7.

The improvement in sintering performance of the $CaTiO_3$-$SmAl_{1-x}Cu_xO_3$ system was observed following the doping of small amounts of Cu (specifically, 0.5 at.%), resulting in a relatively high quality factor. However, the quality factor exhibits a decline with increasing Cu doping concentrations. Hence, excessive doping of Cu ions is not recommended. From SEM imaging shown in Fig. 4 and average grain size in Table 3, the grain size is much smaller with higher doping content. This indicates that the quality factor of the $CaTiO_3$-$SmAl_{1-x}Cu_xO_3$ system is dominated by the grain boundary defects.

The $CaTiO_3$-$SmAl_{1-x}Zn_xO_3$ system exhibited the highest quality factor among all specimens at 1.0 at.% doping concentration with $Q\times f$ reaching 44700 GHz. To further understand the reasons behind the high quality factor associated with Zn doping concentration and its correlation with the solid solution's structure, Raman spectroscopy was conducted as illustrated in Fig. 5b. Given the presence of two or more cations at the B-site of the perovskite structure, understanding the degree of ordering at the B-site is crucial. In the Raman spectra, the A_{1g} peak reflects the degree of short-range ordering at the B sites. The full width at half maximum (FWHM) of the A_{1g} peak was calculated (insets in Fig. 5), since FWHM serves as an indicator of the degree of ordering at B sites, with a smaller FWHM indicating better ordering, leading to a high $Q\times f$ value. The observed decrease in FWHM for the sample with 1.0 at.% Zn (Fig. 5b) aligns with the $Q\times f$ measurement (Fig. 7b) and confirms that Zn doping contributes to an increase in the quality factor at 1.0 at.% doping level. Another contributing factor to the high quality factor of the $CaTiO_3$-$SmAl_{0.99}Zn_{0.01}O_3$ is the B-site bond valence. It has been reported that larger B-site bond valence indicates larger bond strengths between the B-site cations and oxygen ions, which decreases anharmonic interactions in the crystal lattice [37]. This is another reason for the improvement of quality factor. Therefore, the $Q\times f$ values of the $CaTiO_3$-$SmAl_{1-x}Zn_xO_3$ are sensitively dependent on the B-site short range ordering and B-site bond strength.

Among the Ni-doped samples, the $CaTiO_3$-$SmAl_{0.995}Ni_{0.005}O_3$ demonstrated good sintering performance, with B-site ion ordering also influencing the quality factor, as evidenced by Raman spectroscopy in Fig. 5c. The FWHM increases with higher Ni doping content and bond valence also reduces as shown in Fig. 7c. Another contributing factor is the smaller grain size and large porosity with high Ni doping concentrations, which introduces a higher amount of defects.

The tilting of the TiO_6 octahedron significantly impacts the temperature coefficient at the resonant frequency. The tolerance factor (t) is crucial in evaluating the degree of oxygen octahedra tilting [38]. To understand the trend of the temperature coefficient with varying amounts of Cu, Zn and Ni ions, the tolerance factor (t) was evaluated. The temperature coefficient of the resonant frequency is significantly influenced by the tolerance factor, which can be calculated by [34]:

$$t = \frac{r_A + r_O}{\sqrt{2}(r_B + r_O)} \tag{9}$$

where r_A, r_B and r_O are the average ionic radii of A-site, B-site and oxygen ions, respectively. The tolerance factor is plotted in Fig. 8 together with the temperature coefficient. It can be clearly observed that the temperature coefficient is well-correlated with tolerance factor. This indicates that high doping levels of Cu, Zn and Ni increase the degree of oxygen octahedra tilting and worsen the temperature stability.

IV. Conclusions

$CaTiO_3$-$SmAlO_3$ ceramics doped with Cu, Zn or Ni ions were prepared by using a thermal decomposition method and sintering at 1370 °C. Structural and morphological analyses confirmed formation of highly dense structure with single orthorhombic phase

(*Pbnm* space group) and well-defined grains ranging approximately from 1.5 to 3.7 μm. Notably, the $CaTiO_3$-$SmAl_{0.99}Zn_{0.01}O_3$ sample, doped with 1.0 at.% Zn, demonstrated outstanding microwave dielectric properties with a high-quality factor ($Q \times f$) of 44700 GHz and a dielectric constant (ε_r) of 39.6. The research established a clear correlation between microstructure and dielectric characteristics, identifying key factors for enhancing the quality factor and minimizing temperature coefficient. This study provides insights for future research, particularly in understanding the microstructural influences on dielectric properties. The findings offer a strong foundation for developing advanced microwave dielectric materials with improved performance.

References

1. M.T. Sebastian, *Dielectric Materials for Wireless Communication.* Elsevier, 2008.
2. M.T. Sebastian, R. Ubic, H. Jantunen, "Low-loss dielectric ceramic materials and their properties", *Int. Mater. Rev.*, **60** [7] (2015) 392–412.
3. Y. Konishi, "Novel dielectric wave-guide components - Microwave applications of new ceramic materials", *Proceedings IEEE*, **79** [6] (1991) 726–740.
4. S.C. Zhou, X.W. Luan, S. Hu, X.J. Zhou, S. He, X. Wang, H. Zhang, X.L. Chen, H.F. Zhou, "Sintering behavior, phase structure and microwave dielectric properties of CeO added $CaTiO_3$-$SmAlO_3$ ceramics prepared by reaction sintering method", *Ceram. Int.*, **47** [3] (2021) 3741–3746.
5. S. Mohapatra, T. Badapanda, R. Barman, T.K. Das, Y. Huang, J. Xiao, S.N. Tripathy, "Understanding of the correlation of structural and microwave dielectric performance of (1-x)$MgTiO_3$-x$CaTiO_3$ ceramics for dielectric resonator antenna applications", *J. Alloys Compd.*, **1003** (2024) 175616.
6. Y. Hu, "Influence of rare earth ion doping on the dielectric properties of $CaTiO_3$-$SmAlO_3$ ceramics", *Process. Appl. Ceram.*, **17** [4] (2023) 347–353.
7. D.W. Wang, S.Y. Zhang, G. Wang, Y. Vardaxoglou, W. Whittow, D. Cadman, D. Zhou, K. Song, I.M. Reaney, "Cold sintered $CaTiO_3$-K_2MoO_4 microwave dielectric ceramics for integrated microstrip patch antennas", *Appl. Mater. Today*, **18** (2020) 100519.
8. Q. Hu, Y.C. Teng, X.F. Zhao, T. Arslanov, Q.Y. Zheng, T. Luo, R. Ahuja, "Temperature stable dielectric properties of Mg_2TiO_4-$MgTiO_3$-$CaTiO_3$ ceramics over a wide temperature range", *Ceram. Int.*, **49** [2] (2023) 1997–2006.
9. C. Du, D. Zhou, R.-T. Li, H.-T. Chen, G.-H. Zhou, B. Tang, M.A. Darwish, S. Xia, Z. Xu, "Fabrication of wideband low-profile dielectric patch antennas from temperature stable 0.65$CaTiO_3$-0.35$LaAlO_3$ microwave dielectric ceramic", *Adv. Electron. Mater.*, **8** [9] (2022) 2101414.
10. S. Uddin, S. Faisal, A. Zaman, V. Tirth, P. Thakur, M. Lal, "Investigation of impact of Zr-doping on the structural and microwave dielectric properties of $CaTiO_3$ ceramics", *Optical Mater.*, **135** (2023) 113358.
11. S.C. Zhou, Q. Wu, H.R. Xu, X.W. Luan, S. Hu, X.J. Zhou, S. He, X. Wang, H.L. Zhang, X.L. Chen, H.F. Zhou, "Synthesis and characterization of reaction sintered $CaTiO_3$-$LnAlO_3$ (Ln = La, Nd) ceramics", *Ceram. Int.*, **47** [22] (2021) 32433–32437.
12. B. Masin, K. Ashok, H. Sreemoolanadhan, "Microwave hybrid sintering of 0.95(MgZn)TiO_3-0.05$CaTiO_3$ ceramics and its microwave dielectric properties", *J. Eur. Ceram. Soc.*, **42** [12] (2022) 4974–4979.
13. A. Zaman, S. Uddin, N. Mehboob, A. Ali, "Structural investigation and improvement of microwave dielectric properties in $Ca(Hf_xTi_{1-x})O_3$ ceramics", *Phys. Scripta*, **96** [2] (2021) 025701.
14. C.J. Pei, H.K. Liu, M. Chen, F. Shang, W.H. Liu, G.G. Yao, J. Liu, P. Liu, F. Wang, H.W. Zhang, "Structural transformation and microwave dielectric properties of $Li_4Mg_2SbO_6F$ ceramics", *Ceram. Int.*, **50** [23] (2024) 51718–51723.
15. Z.Q. Zhang, R.X. Feng, B. Li, "A novel microwave dielectric ceramic CaB_2O_4 with low dielectric constant", *Physica B*, **695** (2024) 416526.
16. L.Z. Ma, Q.B. Du, G. Tian, H.Z. Xiao, L.X. Jiang, H. Li, "Microwave dielectric properties of novel $Mg_3Ga_2TiO_8$ ceramic", *Ceram. Int.*, **50** [23] (2024) 50774–50779.
17. Z.H. Lin, Y.M. Lai, M.H. Li, J.Q. He, M.W. Li, J. Zhou, S.Q. Li, W.H. Qi, J. Han, Y.M. Zeng, "Effect of TiO_2 doping on microstructure and microwave dielectric properties of $CaNb_2O_6$ ceramics", *J. Alloys Compd.*, **1010** (2025) 177717.
18. Q. Yuan, S. Wang, G. Liu, S. Yan, "Effects of Ta^{5+} substitution on mechanical and microwave dielectric properties of $R(Nb_{1-x}Ta_x)_2O_6$ ceramics", *J. Alloys Compd.*, **1010** (2025) 177428.
19. P.W. Xiang, Y.M. Lai, L.Q. Zhang, F. Liu, Y.X. Li, J. Han, Y.M. Zeng, Q. Liu, C.S. Wu, "Microwave dielectric properties of high-entropy $[(Mg_{1/2}Zn_{1/2})_{0.4+x}(Ni_{1/3}Co_{1/3}Mn_{1/3})_{0.6-x}]_2TiO_4$ ceramics", *J. Alloys Compd.*, **1010** (2025) 177833.
20. T. Jiang, W. Yang, W. Deng, Z. Yu, W. Wen, "Improvement of microstructure and dielectric properties of $Zn_{1.8}SiO_{3.8}$ ceramics by doping with rare earth elements (La, Pr, Nd, Sm)", *J. Alloys Compd.*, **1010** (2025) 177679.
21. H.M. Rietveld, "A profile refinement method for nuclear and magnetic structures", *J Appl. Crystallography*, **2** [2] (1969) 65–71.
22. B.H. Toby, "*EXPGUI*, a graphical user interface for *GSAS", J. Appl. Crystallography*, **34** [2] (2001) 210–213.
23. R. Ali, M. Yashima, "Space group and crystal structure of the perovskite $CaTiO_3$ from 296 to 1720 K", *J. Solid State Chem.*, **178 [**(9] (2005) 2867–2872.
24. L. Vasylechko, A. Senyshyn, U. Bismayer, "Perovskite-type aluminates and gallates", pp. 113–295 in *Handbook on the Physics and Chemistry of Rare Earths*, Vol. 39, Elsevier, 2009.
25. Y.C. Liou, Y.-C. Liou, C.-T. Wu, Y.-L. Huang, T.-C. Chung, "Effect of CuO on $CaTiO_3$ perovskite ceramics prepared using a direct sintering process", *J. Nuclear Mater.*, **393** [3] (2009) 492–496.
26. C.L. Huang, J.L. Hou, C.-L. Pan, C.-Y. Huang, C.-W. Peng, C.-H. Wei, Y.-H. Huang, "Effect of ZnO additive on sintering behavior and microwave dielectric properties of 0.95$MgTiO_3$-0.05$CaTiO_3$ ceramics", *J. Alloys Compd.*, **450** [1-2] (2008) 359–363.
27. V. Zelezny, E. Cockayne, J. Petzelt, M.F. Limonov, D.E. Usvyat, V.V. Lemonov, A.A. Volkov, "Temperature dependence of infrared-active phonons in $CaTiO_3$: A combined spectroscopic and first-principles study", *Phys. Rev. B*, **66**

[22] (2002) 224303.
28. Y. Li, S. Qin, F. Seifert, "Phase transitions in A-site substituted perovskite compounds: The $(Ca_{1-2x}Na_xLa_x)TiO_3$ ($0 \leq x \leq 0.5$) solid solution", *J. Solid State Chem.*, **180** [3] (2007) 824 –833.
29. H. Zheng, G.D.C. Csete de Györgyfalva, R. Quimby, H. Bagshaw, R. Ubic, I.M. Reaney, J. Yarwood, "Raman spectroscopy of B-site order-disorder in $CaTiO_3$-based microwave ceramics", *J. Eur. Ceram. Soc.*, **23** [14] (2003) 2653–2659.
30. H. Zheng, L.M. Reaney, G.D.C. Csete de Györgyfalva, R. Ubic, J. Yarwood, M.P. Seabra, V.M. Ferreira, "Raman spectroscopy of $CaTiO_3$-based perovskite solid solutions", *J. Mater. Res.*, **19** [2] (2004) 488–495.
31. S.J. Penn, N.M. Alford, A. Templeton, X. Wang, M. Xu, M. Reece, K. Schrapel, "Effect of porosity and grain size on the microwave dielectric properties of sintered alumina", *J. Am. Ceram. Soc.*, **80** [7] (1997) 1885–1888.
32. R.D. Shannon, "Dielectric polarizabilities of ions in oxides and fluorides", *J. Appl. Phys.*, **73** [1] (1993) 348–366.
33. J.Y. Hao, J. Guo, E. Zhao, M. Si, X. Yuan, F.-Z. Yao, H. Wang, "Grain size effect on microwave dielectric properties of Na_2WO_4 ceramics prepared by cold sintering process", *Ceram. Int.*, **46** [17] (2020) 27193–27198.
34. H.J. Jo, E.S. Kim, "Effect of Sn^{4+} substitution on microwave dielectric properties of $(Mg_{0.95}Ni_{0.05})(Ti_{1-x}Sn_x)O_3$ ceramics", *Mater. Res. Bull.*, **67** (2015) 221–225.
35. I.D. Brown, D. Altermatt, "Bond-valence parameters obtained from a systematic analysis of the inorganic crystal-structure database", *Acta Crystallogr. B*, **41** (1985) 244–247.
36. G.J. Palenik, "Bond valence sums in coordination chemistry. The calculation of the oxidation state of samarium in complexes containing samarium bonded only to oxygen", *Inorg. Chem.*, **42** [8] (2003) 2725–2728.
37. J.M. Li, Y. Han, T. Qiu, C. Jin, "Effect of bond valence on microwave dielectric properties of (1-x)$CaTiO_3$-x$(Li_{0.5}La_{0.5})TiO_3$ ceramics", *Mater. Res. Bull.*, **47** [9] (2012) 2375–2379.
38. J.J. Qu, F. Liu, C.L. Yuan, X.Y. Liu, G.H. Chen, "Effects of Bi^{3+} substitution for Nd^{3+} on microwave dielectric properties of $Ca_{0.61}(Nd_{1-x}Bi_x)_{0.26}TiO_3$ ceramics", *Mater. Lett.*, **159** (2015) 436–438.